

Ionized Absorbers in AGN: the role of collisional ionization and time-evolving photoionization

Fabrizio Nicastro^{1,2}, Fabrizio Fiore^{1,2,3}, G. Cesare Perola⁴, Martin Elvis¹

¹ Harvard-Smithsonian Center for Astrophysics

60 Garden St, Cambridge MA 02138

² Osservatorio Astronomico di Roma

via Osservatorio, Monteporzio-Catone (RM), I00040 Italy

³ SAX Science Data Center

via Corcolle 19, Roma I00100 Italy

⁴ Dipartimento di Fisica, Università degli studi “Roma Tre”

Via della Vasca Navale 84, Roma, I00146 Italy

version: 3:00pm, 20 June 1998

ABSTRACT

In this paper we explore collisional ionization and time-evolving photoionization in the, X-ray discovered, ionized absorbers in Seyfert galaxies. These absorbers show temporal changes inconsistent with simple equilibrium models. We develop a simple code to follow the temporal evolution of non-equilibrium photoionized gas. As a result several effects appear that are easily observable; and which, in fact, may explain otherwise paradoxical behavior.

Specifically we find that:

1. In many important astrophysical conditions (OVII, OVIII dominant; and high ($\gtrsim 10^{22.5} \text{cm}^{-2}$) column density) pure collisional and photoionization equilibria can be distinguished with moderate spectral resolution observations, due to a strong absorption structure between 1 and 3 keV. This feature is due mainly to iron L XVII-XIX and Neon K IX-X absorption, which is much stronger in collisional models. This absorption structure may be misinterpreted as a flattening of the intrinsic emission spectrum above ~ 1 keV in low resolution data.
2. In time-evolving non-equilibrium photoionization models the response of the ionization state of the gas to sudden changes of the ionizing continuum is smoothed and delayed at low gas densities (usually up to 10^8cm^{-3}), even when the luminosity increases. The recombination time can be much longer (up to orders of magnitude) than the photoionization timescale. Hence a

photoionized absorber subject to frequent, quick, and consistent changes of ionizing luminosity is likely to be overionized with respect to the equilibrium ionization state.

3. If the changes of the ionizing luminosity are not instantaneous, and the electron density is low enough (the limit depends on the average ionization state of the gas, but is usually $\sim 10^7 \text{ cm}^{-3}$ to $\sim 10^8 \text{ cm}^{-3}$), the ionization state of the gas can continue to increase while the source luminosity decreases, so a maximum in the ionization state of a given element may occur during a minimum of the ionizing intensity (the opposite of the prediction of equilibrium models).
4. Different ions of different elements reach their equilibrium configuration on different time-scales, so models in which all ions of all elements are in photoionization equilibrium so often fail to describe AGN spectral evolution.

These properties are similar to those seen in several ionized absorbers in AGN, properties which had hitherto been puzzling. We applied these models to a high S/N ROSAT PSPC observation of the Seyfert 1 galaxy NGC 4051. The compressed dynamical range of variation of the ionization parameter U and the ionization delays seen in the ROSAT observations of NGC 4051 may be simply explained by non-equilibrium photoionization model, giving well constrained parameters: $n_e = (1.0_{-0.5}^{+1.2}) \times 10^8 \text{ cm}^{-3}$, and $R = (0.74_{-0.40}^{+0.80}) \times 10^{16} \text{ cm}$ (~ 3 light days).

1. INTRODUCTION

The detection and the study of ionized absorbers is more difficult than that of cold neutral absorbers, but can yield much more detailed information about the nature of the absorbers and the state and geometry of the nuclear regions of AGN. If photoionization applies then the electron density of the gas and its distance from the ionizing source can be estimated.

Absorption features from ionized gas, are common in the X-ray spectra of Seyfert Galaxies and some quasars ¹. Deep oxygen VII and VIII absorption edges at 0.74 keV and 0.87 keV (rest) have been detected by the ROSAT PSPC and the ASCA SIS in quite a large number of Seyfert 1 galaxies (Reynolds, 1997).

We do not know yet what is the origin of the gas ionization. Models to date have assumed the simplest equilibrium photoionization case (e.g. Fiore et al., 1993; Guainazzi et al., 1996; Reynolds et al., 1995). In this case, if the gas is confined in a single cloud of constant density, and if the recombination time is smaller than the typical variability timescale, then the ionization parameter, and hence the ionization state of the gas, should follow closely the intensity of the ionizing continuum. This is not always observed. In two ASCA observations of MGC-6-30-15 (Fabian et al. 1994, Reynolds et al. 1995) the best fit ionization parameter is higher when the ionizing flux is lower, in contrast with the expectations of the simplest equilibrium photoionization model; the ASCA observations of MR2251-178 show a roughly constant ionization parameter despite large variation in the 2-10 keV flux (Reynolds & Fabian, 1995); finally, in a ROSAT observation of NGC 4051 (McHardy et al., 1995), the ionization parameter does not linearly track the luminosity, but shows changes that are smoothed and delayed with respect to the luminosity changes. It seems clear that, at least in the above three cases (which are also the best studied), the simplest photoionization equilibrium model is inadequate. We clearly need more complete and consistent models to interpret the available data. The gas could well be distributed in an irregular region with varying density. Different ionization states would then apply to different region of this gas. Other authors have adopted such multi-zone models (Otani et al. 1996, Kriss et al. 1996). In those models the authors assume that absorption features

¹ NGC 4051: Mc Hardy et al. 1995; Guainazzi et al., 1996; MGC-6-30-15: Nandra & Pounds, 1992, Reynolds et al. 1995, Orr et al., 1997; NGC 3783: Turner et al. 1993, George et al., 1996, George et al., 1998; NGC 985, Brandt et al. 1994, Nicastro et al., 1997; NGC 5548: Done et al. 1995, Mathur et al. 1995; NGC 3227, Ptak et al. 1994; NGC 3516, Kriss et al. 1996; IC 4329A, Cappi et al. 1996; PG 1114+445: Laor et al. (1997), George et al., 1997, Mathur et al., 1998; MR 2251–178, Halpern (1984), Pan, Stewart and Pounds (1990); 3C 351, Fiore et al. (1993), Nicastro et al., 1998; see also Reynolds (1997)

from different ions of the same element are imprinted on the spectrum by the transmission of the ionizing radiation through multiple distinct clouds of gas with different geometrical configurations, ionization states and densities. This is of course a possibility, but to us it seems rather ‘ad hoc’.

In this paper instead we discuss the additional physics of collisional ionization, and of time-evolving photoionization in a single zone model. Time-evolving photoionization models have been applied in the past to the extended narrow line emitting region of radio galaxies, to predict the evolution of the line ratios in low-density ($n_e = 1 \text{ cm}^{-3}$), low ionization ($\text{Log}U \sim -3$), multi-zone photoionized gas after the switch-off of the ionizing source (Binette et al., 1987). We present here an iterative solution of the time-dependent ionization balance equations (accounting for all ions of the most abundant elements in gas with solar composition), and apply our models to a drastically different physical and geometrical configuration: a relatively high-density ($n_e = 10^6 - 10^9 \text{ cm}^{-3}$), medium-high gas ionization ($\text{Log}U \sim -1, 1$), geometrically thin ($\Delta R/R \sim 10^{-3}$), single zone absorber along the line of sight, undergoing rapid and persistent variations of the ionizing flux.

As an example, we apply our models to the ROSAT data of the Seyfert 1 galaxy NGC 4051. A detailed analyses of the time behaviour of ionized gas in Seyfert 1 galaxies, using the ASCA-SIS relatively high resolution data, is deferred to a future publication.

2. Ionization Models

The innermost regions of an AGN are likely to be ‘active’, in the sense that the gas there confined is expected to be involved in significant bulk motion, as in strong outflows (Arav et al., 1995) or inflows. In particular the evidence for ionized outflows from the central regions of AGN is strong (Mathur et al. 1994, 1995, 1997, 1998). Hence sources of mechanical heating of the gas (for example adiabatic compression by shock waves) may well be at work in the high density clouds, making collisional ionization the dominant ionization mechanism. In the low density clouds the gas could be far from photoionization equilibrium, because the recombination timescales have become greater than the X-ray continuum variability timescales. Hereinafter, by *photoionization time* (t_{ph}) and *recombination time* (t_{rec}) we mean the time necessary for the gas to reach photoionization equilibrium with the ionizing luminosity during increasing and decreasing phases respectively. We discuss in turn the possible importance of collisional ionization and time-evolving photoionization, in determining the final transmitted spectrum that we observe in AGN.

2.1. Collisional Ionization Models

To study collisional ionization we constructed a series of pure collisional ionization models and compared them with the equilibrium photoionization models. The models were created using CLOUDY (version 90.01, Ferland, 1996), fixing the ionization parameter (i.e. the dimensionless ratio between the number of Hydrogen ionizing photons and the electron density of the gas) U to 10^{-5} and calculating the spectra transmitted through clouds with a total column density, $N_H = 10^{22.5} \text{ cm}^{-2}$, constant density and temperature (the calculation of the physical condition of clouds in coronal or collisional equilibrium is one of the options of CLOUDY; Ferland, 1996). The distribution of fractional abundances for the most important ions is essentially independent of the electron density value: for $10 < n_e < 10^{12} \text{ cm}^{-3}$; the variation is smaller than 13% for ions with fractional abundances greater than 0.01.

For temperatures T_e in the range $10^5 - 10^{7.1}$ the main edges imprinted on the spectra are roughly the same as those in the spectra from photoionized gas with $-1 < \log(U) < 1.5$. However, the distribution of the different ionic species is very different in the two cases, and so the relative optical depth of the edges differ markedly. High quality X-ray spectra, where more than one edge is visible, could then discriminate between the two cases.

The different ionic abundances in the collisional and photoionized cases can be seen in Figs. 1a,b and 2a,b. Here we plot the fractional abundances of NeVIII-NeXI and OVI-OIX (Fig. 1) and FeXIV-FeXXV (Fig. 2), computed in the case of photoionization and collisional ionization respectively as a function of U and T_e . As Fiore et al (1993) and Mathur et al. (1994) have shown, the photo-ionization state of the gas depends strongly on the spectral energy distribution (SED) of the ionizing continuum, from radio to hard X-rays. To simplify the comparison between photoionization models and the data, we therefore used an ionizing continuum similar to the SED of NGC 4051 (Done et al 1990).

Firstly we note that the fractional abundances in photoionized gas are more smoothly distributed than those of collisionally ionized gas. Let us consider the regime in which the OVII and OVIII fractions are higher than ≈ 0.2 , so that both OVII and OVIII edges are present in the emerging spectrum, as sometimes found in Seyfert galaxies spectra (e.g. Otani et al. 1996, Guainazzi et al. 1996). In the photoionization case the range of U where this occurs is 1.2–3.6, a factor 3. This is twice as wide as the corresponding range of T_e : $1.5 \times 10^6 - 2.4 \times 10^6 \text{ K}$ (a factor of 1.6: dotted lines in panels *a* and *b* of Fig. 1). Moreover, NeIX is abundant and Carbon is almost fully stripped in the collisional case, but not in the photoionized case.

The difference in the resulting spectra is shown in Fig. 3a. Here we show the ratio between two power law spectra emerging respectively from clouds of collisionally ionized

($T_e = 1.8 \times 10^6$ K) gas, and photoionized (U=2) gas with solar abundances (the choices of T_e and U were made by looking for similar OVII-OVIII abundances: see Fig. 1a). Below 1 keV there is a large feature due to the deep CVI K absorption edge in the photoionization case. The most important feature above 1 keV is the NeIX absorption edge in the collisional case, but this feature is smoothed by the presence, in both cases, of deep OVII and OVIII absorption edges. Reynolds (1997), fitted both a simple OVII and OVIII K-edges model and a physical photoionization model to ASCA SIS spectra of a sample of Seyfert 1 known to host a warm absorber. Comparing the results he found that in some cases, the best fit 2-edges model continue to show residuals at the energy of CVI K edge, while residuals to physical photoionization model do not. This may point to photoionization as ionizing mechanism. Spectra with higher resolution from 0.4 keV to 3 keV should therefore allow one to diagnose absorption by collisionally ionized or photoionized gas that has significant OVII and/or OVIII abundances (e.g. Otani et al. 1996, Guainazzi et al. 1996).

The other important feature of collisional models is the inertia of the heavy elements (from Ne to Fe) against becoming highly ionized, even when the oxygen is almost fully stripped. In Fig. 1a and 1b we have marked the range of U for which OIX is by far the dominant ion ($n_{OIX} \gtrsim 0.8$) and OVIII is the only oxygen edge in the emergent spectrum ($\tau \lesssim 0.8$, for an N_H of $10^{22.5}$ cm $^{-2}$ and solar abundances). These same intervals of U and T_e are also shown in Fig 2a and 2b. In the photoionization case Neon is almost fully stripped (NeXI), and the dominant ions of the iron are FeXVIII to FeXXIII. Instead in the collisional case there is a range of temperature for which Neon and Iron are much less ionized, with the dominant ions being NeIX-NeX, and FeXVI to FeXX. In particular we note the large abundance of FeXVII (FeXVII and FeXXV are respectively Ne-like and He-like, and so very stable). The different ionization level of Neon and Iron implies a very different emergent spectrum between 1 and 3 keV.

This is illustrated in Fig. 3b which shows the ratio between spectra transmitted from collisionally ionized gas with $T_e = 3.9 \times 10^6$ K, and photoionized gas with U=10 (both with $N_H = 10^{22.5}$ cm $^{-2}$). With these values of T_e and U, $n_{OIX} \sim 0.8$ in both collisional ionization and photoionization models (see Fig. 1a). The ratio does not show any significant feature at $E < 1$ keV (implying similar ionization states of Carbon, Nitrogen and Oxygen), but between 1 and 3 keV, the spectrum from collisionally ionized gas shows a large and complicated absorption structure due mainly to iron L XVII-XIX and Neon K IX-X absorption (Fig. 3b). This absorption structure may be mis-interpreted in moderate quality spectra as a flattening above ~ 1 keV. Again, higher spectral resolution data with good S/N can distinguish between photoionization or collisional equilibrium.

That the NeIX and FeXVII edges are of similar depth is due to a coincidence of cross-

sections and abundances. The photoelectric cross section of the iron L shell atoms ranges from $\sim 2 \times 10^{-19}$ cm² for the Lp levels of FeXVI-FeXIX ($E \sim (1.17-1.47)$ keV), to $\sim 3 \times 10^{-20}$ cm² for the Lp level of FeXXII ($E=1.78$ keV) (Kallman & Krolik, 1995).² Furthermore in the collisional case the relative abundance of FeXVII is in the range 0.2–0.7, compared to $\lesssim 0.25$ in the analogous photoionization case. The relative abundance of the NeX, in the collisional case, is greater than 0.25, but NeX $\lesssim 0.4$ in the analogous photoionization case, while $0.05 \lesssim (\text{NeIX})_{\text{Coll}} \lesssim 0.40$ and $(\text{NeIX})_{\text{Phot}} \lesssim 0.05$ (Fig. 1 a,b). The K-edge energy of NeX is 1.36 keV the same of that of the FeXVIII Lp-edge. While the photoelectric cross-section of Neon is about a factor 4 lower than Iron, the solar abundance of the Neon is about a factor 4 greater than that of Iron (Grevesse & Anders 1989). Furthermore the cross-section of NeIX is about a factor 3 higher than NeX. As a result, spectra from a cloud of collisional ionized gas at $T_e \sim 4 - 6 \times 10^6$ K, will show a very deep ($\tau_{\text{Fe}^{L_P\text{XVII}}} \sim 1.0 \times N_{H_{23}}$) edge at the FeXVII Lp-edge energy (1.26 keV), a deep ($\tau_{\text{Fe}^{L_P\text{XVIII}} + \text{Ne}^{K_X}} \sim 0.7 \times N_{H_{23}}$) edge at 1.36 keV due to the comparable contributions of the NeX K-edge and the FeXVIII Lp-edge, and a similarly deep absorption edge at the NeIX K-edge energy ($E^K(\text{NeIX}) = 1.196$ keV, $\tau_{\text{Ne}^{K_{IX}}} \sim 0.6 \times N_{H_{23}}$). In the corresponding photoionization case, the relative abundances of both NeIX-X and FeXVII-XVIII are too low (Fig. 1a,b, 2a,b) to imprint similar features on the spectrum.

When collisions are the dominant ionization process, ($U \lesssim 0.01$) we can estimate the minimum distance, R , between the ionized gas cloud and the central source. For an ionizing luminosity L_{ion} , we find: $R > 1.6 \times 10^{16} (n_{e_{10}})^{-0.5} (Q_{52})^{0.5}$ (with $n_{e_{10}}$ being the electron density in units of 10^{10} cm⁻³, and Q_{52} the rate of photons ionizing hydrogen in units of 10^{52} ph s⁻¹: $Q = \int_{E_{Ly}}^{\infty} dE (L_{\text{ion}}(E)/E)$). For typical AGN ionizing continuum shapes and luminosities ($L_{\text{ion}} = 10^{42}, 10^{45}$ erg s⁻¹), and assuming $n_{e_{10}} = 1$, we find $R > 6.2 \times 10^{16}$ cm, 2×10^{18} cm, respectively, similar to the size of the BLR for such AGN (Peterson et al., 1993).

2.2. Mixed Collisional and Photoionization Models

The above discussion concerns gas in pure collisional equilibrium. If the gas density is low enough and/or if the gas is close enough to the central X-ray source then photoionization can be important too. We examined a number of models with a varying mixture of collisional

²The photoelectric cross section of the Ls levels of the iron ions, is about one order of magnitude lower than the corresponding Lp cross sections, and the Lp levels of the ions FeXXIII-FeXXVI are not populated in ordinary conditions.

ionization and photoionization. For $T_e = 2.5 \times 10^6$ we find that for values of $U \lesssim 0.1$ the main features of the fractional abundance distribution are still those of pure collisional ionized gas. Increasing U to 0.3 causes a sharp change in the ionization structure. For $0.3 < U \lesssim 100$ (the exact value of the upper limit depending on the equilibrium temperature determined by collisional mechanisms) the ionization structure is determined by *both* processes, and the transmitted spectra resemble those from pure photoionized gas of *much higher* ionization parameter. This is shown in Fig. 4 where we plot in the lower panel three spectra from purely photoionized gas (column density $\log N_H = 22.5$ and $\log(U) = 0.7, 1.1$ and 1.4), and in the upper panel 5 spectra from gas in which both mechanisms are at work ($\log N_H = 22.5$, $T_e = 2.5 \times 10^6$ and $\log(U) = -2, -1, 0.3, 0, 0.4$). The pure photoionization spectra with $\log(U) = 0.7, 1$ (lower panel) are very similar to the mixed collisional and photoionization spectra with a factor 4-10 times lower U ($\log(U) = -0.3, 0.4$; upper panel). Fitting the mixed spectra with pure photoionization models would give a much more compressed range of U than the real one, as found by McHardy et al. in NGC 4051. The above spectra in the two panels of Fig. 5 are practically undistinguishable even at high resolution, because the shape of the fractional abundance distributions when both processes are working, closely resemble those of a purely photoionized gas (see upper panels of Fig. 1 and 2). Fortunately the two models predict quite different delay properties (§2.3).

2.3. Time-evolving Photoionization Models

If photoionization is the dominant process (the gas being purely photoionized, or the density enough low to give $U \gtrsim 0.1$) the main features of the fractional abundance distribution are those of photoionized gas. However, if the X-ray source is variable, photoionization equilibrium will apply only if the density is high enough to make the ion recombination timescales shorter than the variability timescales. There are regimes where photoionization equilibrium does not apply at all. Here we investigate the low density case in some detail, beginning with a discussion of the relevant physics.

2.3.1. Equilibrium photoionization

Let us suppose that a geometrically thin single cloud of optically thin, gas is illuminated by an intense flux of ionizing radiation emitted by a variable source located at a distance R from the cloud.

We can calculate the equilibrium distribution of the ionic species in the cloud, by setting the photoionization rate equal to the radiative recombination rate ³ (see, e.g., Netzer, 1990).

$$(1) \quad \left(\frac{n_{X^{i+1}}}{n_{X^i}} \right)^{eq} = \frac{F_{X^i}}{\alpha_{rec}(X^i, T_e)n_e},$$

and adding the condition for charge conservation $\sum_i n_{X^i} = 1$. Here $\alpha_{rec}(X^i, T_e)$ is the radiative recombination coefficient (in $\text{cm}^3 \text{s}^{-1}$), which includes recombination to all levels, and F_{X^i} is the photoionization rate of the ion X^i , which, for optically thin gas clouds, can be written (see, eg., Netzer, 1990):

$$(2) \quad F_{X^i} = \frac{1}{4\pi R^2} \int_{\nu_{X^i}}^{\infty} d\nu \frac{L_\nu}{h\nu} \sigma_\nu(X^i).$$

The lower limit of the integral is the threshold ionization frequency of the ion X^i . $\sigma_\nu(X^i)$ is the photoelectric absorption differential cross section of the ion X^i .

In this simple scheme the ionization state of the gas is completely determined, at equilibrium, by the value of the ionization parameter $U = F_{HI}/n_e c$. ⁴

With these approximations the ionization parameter U can be written as a function of the ratio between any two consecutive ionic species of the generic element X :

$$(5) \quad U = \left(\frac{n_{X^{i+1}}}{n_{X^i}} \right) \left(\frac{F_{HI}}{F_{X^i}} \right) \frac{\alpha_{rec}(X^i, T_e)}{c}.$$

³Neglecting the normally small effects of Auger ionization, collisional ionization and three body recombination.

⁴The inverse of the photoionization and radiative recombination rates are usually referred in the literature as the photoionization and recombination times:

$$(3), (4) \quad t_1^{X^i} = \frac{1}{F_{X^i}}, \quad t_2^{X^i} = \frac{1}{\alpha_{rec}(X^i, T_e)n_e}.$$

Instead in this paper we refer to different quantities as *photoionization* time and *recombination* time: see eq. 7.

2.3.2. Time-evolving photoionization: Equations

If the gas is not in equilibrium eq. 5 is of course meaningless. However, it is still possible to use it formally by introducing an ionization parameter $U^{X^i, X^{i+1}}(t)$ which depends both on time *and* on the specific ionic species under consideration.

The time evolution of the relative density of the ion i of the element X , considering only radiative recombination and photoionization, is then given by (Krolik and Kriss, 1995):

$$(6) \quad \frac{dn_{X^i}}{dt} = - \left[F_{X^i} + \alpha_{rec}(X^{i-1}, T_e) n_e \right] n_{X^i} + F_{X^{i-1}} n_{X^{i-1}} + \alpha_{rec}(X^i, T_e) n_e n_{X^{i+1}}.$$

The first term on the right of eq. 6, is the *destruction rate* of the ion X^i , both by photoionization $X^i \rightarrow X^{i+1}$ and radiative recombination $X^i \rightarrow X^{i-1}$, while the other two terms indicate the *formation rate* of the ion X^i by photoionization of the ion X^{i-1} and radiative recombination of the ion X^{i+1} respectively.

The solution of eq. 6 is a system of N coupled integral equations in the N unknowns n_{X^i} , which is analytically solvable only for $N=2$, with the addition of the charge conservation condition. These solutions define the time scale t_{eq} , that measures the time necessary for the gas to reach photoionization equilibrium with the ionizing continuum. This time is given at any point of the light curve of the ionizing continuum by the inverse of the destruction rate of the ion X^i (following Krolik & Kriss 1995). A useful analytical approximation for t_{eq} is:

$$(7) \quad t_{eq}^{X^i, X^{i+1}}(t \rightarrow t + dt) \sim \left[\frac{1}{\alpha_{rec}(X^i, T_e)_{eq} n_e} \right] \left[\frac{1}{\left(\frac{\alpha_{rec}(X^{i-1}, T_e)}{\alpha_{rec}(X^i, T_e)} \right)_{eq} + \left(\frac{n_{X^{i+1}}}{n_{X^i}} \right)_{eq}} \right]_{t+dt},$$

where eq indicates the equilibrium quantities. During increasing ionization flux phases we call $t_{eq}^{X^i, X^{i+1}}$ *photoionization time*, t_{ph} ; during decreasing ionization flux phases we call $t_{eq}^{X^i, X^{i+1}}$ *recombination time*, t_{rec} . These times are generally different from t_1 and t_2 in eq. 3 and 4.

Equation 7 shows that the time $t_{eq}^{X^i, X^{i+1}}(t \rightarrow t + dt)$ necessary for the gas to reach equilibrium depends explicitly on the electron density n_e in the cloud, and on the equilibrium ratio between two consecutive ionic species calculated at the time $t+dt$. This is the key result of this work, which has major consequences:

1. the time scale on which the gas reaches equilibrium with the ionizing continuum depends on the electron density, *even when the continuum increases* (Fig. 5);
2. different ions reach their equilibrium relative abundances at different points of the light curve (Fig. 6);
3. if changes of intensity are not instantaneous ($dL/dt < \infty$), the time behavior of the relative abundance of a given ion can be opposite to that of the ionizing source (Fig. 6).

All of these effects have been seen in ionized absorbers in AGN. Using these effects non-equilibrium photoionization models can strongly constrain the physical state of the absorber.

2.3.3. Time-evolving Photoionization: Calculations

We created a program to solve the first order differential equation system of eq. 6 for all the ions of the elements H, He, Li, C, N, O. The program uses an iterative method (see Gallavotti, 1983), that permits the solution of any system of N first order differential equations in the N unknowns x_i , of the form $\dot{\mathbf{x}}(\tau) = \mathbf{f}(\mathbf{x}(\tau))$, ($\forall \tau > 0$), with the only conditions being that $f_i \in C^\infty$ and a limited ensemble Ω exists, such that $x_i \in \Omega$.

We consider the photoionization from the K-shell of each element, and radiative recombination to all levels for each ion.

We use the recombination rates tabulated by Shull and Van Steenberg (1982) for the metals. We take the values of the recombination rate of hydrogen from Ferland (1996); we get the total recombination rate by summing over levels $n=1,20$. We calculate the photoionization rate from the K-shell of each ion, carrying out the integrals in eq. 2, using for the spectral shape of the ionizing continuum, from the Lyman limit to γ -rays, a simple power law with $\alpha = 1.3$ (similar to the observed SED of NGC 4051). We use the photoelectric K-shell cross section tabulated by Kallman and Krolik (1995).

We carry out the calculation of the time-evolving heating-cooling balance, as described below. We calculate with CLOUDY (Ferland, 1996) a grid of models for 300 values of U (from 0.01 to 100), and build the curve $U=U(T_e)$, using the technique described in Kallman and Krolik (1995). We then interpolate on these, to obtain the initial self-consistent equilibrium electron temperature of the gas. The time evolution of the temperature in the cloud is carried

out performing an iterative calculation of the time dependent photoionization equations, using the definition of $U^{X^i, X^{i+1}}(t)$ given above.

The inputs the program needs are: (a) the initial equilibrium value of the ionization parameter U ; (b) the spectral shape of the ionizing continuum; (c) the light curve of the ionizing continuum; (d) the electron density n_e ; (e) the ratio, P , between the source intensity and the intensity the source should have in order to produce the observed degree of ionization, assuming equilibrium at the beginning of the light curve.

The output of the program is a list of the relative ionic abundances of the chosen element, and the source flux at the illuminated face of the cloud as a function of time.

2.3.4. *Limits of the code*

We neglect photoionization from the L-shell. This affects the computation of the abundance balance when the gas is allowed to recombine to medium-to-low ionization states, with the Li-like ions (or lower) being highly populated. However this is not likely to be the case for warm absorbers in AGN, for which the mean degree of ionization is usually very high, and the most abundant element (C to Ne) are almost equally distributed between He-like and fully stripped ions (see Fig. 1a). Our code can provide accurate results only at medium-high ionization regimes, those of interest for the astrophysical problem discussed in this paper.

We have also neglected Iron ions. This will likely cause an overestimation of the OVII-IX and NeIX-XI K-shell photoionization, since all these ions compete for the same photons. By comparing the OVII-IX, NeIX-XI equilibrium abundances obtained with our method with those obtained with CLOUDY for U in the range 0.1-50 we estimate that the percentage differences are smaller than 7 %

The iterative technique presented in the previous section is only an approximation to the correct self-consistent time-evolving heating-cooling calculation accounting for all the physical and dynamical heating-cooling mechanisms. We verified that for high gas electron densities (and therefore in a situation close to equilibrium) this method is rather accurate. By comparing the equilibrium relative abundances of the main ions obtained with our method with that obtained using CLOUDY we estimate that for U in the range 0.1-50 the method works with a precision better than 10%. In the opposite case, when the density is sufficiently low, the gas remains basically in the same state and does not respond to variation of the ionizing continuum. Of course in this case our approximation is also very good, albeit

uninteresting. In the intermediate cases, when the heating timescale may be longer than the typical photoionization timescale, the recombination rate coefficients may be greater than those estimated by our assumption. We have tried to estimate the magnitude of the uncertainty on the ion abundance distribution induced by this effect by performing the time-evolving calculations fixing the temperature at a constant value equal to the initial value, and letting the ionizing intensity be free to vary by a factor of 10. For an average gas ionization state typical of AGN warm absorbers ($U = 0.1-50$), the percentage difference between the relative abundances of the main ions calculated with the iterative solution of the time dependent photoionization equations, and those calculated for a gas with a constant temperature are $\lesssim 15 - 20\%$. The difference is so small because of the rather small dynamic range spanned by the temperature in a photoionized gas with $U=0.1-50$ ($3 \times 10^4 \lesssim T_e \lesssim 3 \times 10^5$) and of the weak dependence of the recombination rates on T_e (about the square root of T_e , see Shull and Van Steenberg, 1982).

Given the configuration of the gas we considered (a thin, plan-parallel slab obscuring the line of sight), and the range of electron and column densities, the light-crossing time is smaller than both the typical source intensity variability timescales and the associated photoionization recombination timescales. We can then neglect the effects of the light-crossing time through the cloud of photoionized gas (see Binette, 1988).

2.3.5. The Step Function Light Curve

The simplest case is that of a two state light curve. Let us suppose that the ionizing continuum intensity goes *instantaneously* from a “low” to a “high” state and comes back to the “low” state after a time t_{var} (Fig. 5a). The time behaviour of the ionization state of the gas irradiated by this continuum depends on the value of the ratio $t_{var}/t_{eq}^{X^i, X^{i+1}}(t \rightarrow t + dt)$, and the amplitude of the flux variation (here we adopt a factor 10 change in flux).

We considered the case of an optically thin cloud of gas with an initial ionization such that the most relevant ionic species of the oxygen are OVIII and OIX (corresponding to equilibrium value of $U \gtrsim 5$ with the adopted SED).

The time behavior of the relative density of n_{OIX} is shown in Fig. 5b. In both panels different lines identify different values of the electron density, $n_e = 10^7, 5 \times 10^7, 10^8, 10^9 \text{ cm}^{-3}$. In the upper panel different n_e imply four values of the distance of the cloud from the ionizing source.

The photoionization time $t_{ph}^{OVIII, OIX}$ (eq. 7) of the gas becomes progressively longer as

the density decreases: from about 3×10^3 s for $n_e = 10^8 \text{ cm}^{-3}$, to $\sim 10^4$ s for $n_e = 5 \times 10^7 \text{ cm}^{-3}$ to even longer timescales for $n_e = 10^7 \text{ cm}^{-3}$ (for $n_e \lesssim 10^6 \text{ cm}^{-3}$ the changes of n_{OIX} during the first 10^4 s are $< 10\%$). Note that this is not true for t_1 in eq. 3, which is the definition of photoionization time usually found in literature.

Formally the dependence of t_{ph} on n_e is introduced by the choice of a particular set of boundary conditions when solving eq. 6, and hence defining $t_{eq}^{X^i, X^{i+1}}(t \rightarrow t + dt)$. Physically, fixing the boundary conditions of the system means to choose a particular initial ionic distribution in the gas, and hence its initial ionization state. Different values of n_e , given the initial ionization state of the gas (and hence the ratio between the flux of ionizing photons at the illuminated face of the cloud and the electron density), imply different distances of the gas from the X-ray source. This is clear in the upper panels of Fig. 5 where the ionizing flux at the illuminated face of the cloud is plotted for different values of n_e .

Recombination times are generally longer ($t_{rec}^{OIX, OVIII} > t_{var}$), and can be order of magnitude longer. At the highest density tested ($n_e = 10^9 \text{ cm}^{-3}$) the ionization state of the gas is able to relax to the initial equilibrium state in less than 10^4 s after the source switch off. Recombination time scales for $n_e \leq 10^8 \text{ cm}^{-3}$ are long, the order of many times 10^4 s. Since the source switch off is instantaneous the relative density of OIX never increases after the switch off.

This case illustrates clearly how photoionization recombination timescales can have a strong effect on the changes observed in ionized absorbers and why the photoionization timescale depends on electron density. In the following section we present a more realistic light-curve, and discuss in detail the main features of our models.

2.3.6. The gradual rise & decay light curve: $dL/dt < \infty$

We now consider a more realistic light curve. In this case the source intensity goes from a low state to a high state in a finite time (4,000 s), and after 2,000 s comes back to the initial low state with the same absolute gradient (Fig. 6a). The entire up & down cycle lasts 10,000 s. As in the previous case the change in flux is a factor 10. The corresponding light curves of the relative abundances of the fully stripped ions of three different elements, CVII, NVIII and OIX, are shown in Fig. 6b. In both panels different lines correspond to different values of the electron density, $n_e = 10^8, 10^9 \text{ cm}^{-3}$.

The gradual changes of the ionizing continuum produce time delays between the source light curve and the relative ion abundance light curves. In the lower density case ($n_e = 10^8$

cm^{-3} solid lines), n_{OIX} reaches its maximum value (well below the equilibrium value ~ 1) around the minimum of the luminosity intensity (at $\sim 10,000$ s). During the whole decreasing luminosity phase n_{OIX} is slightly increasing or constant. X-ray spectra taken during the high luminosity phase and the decreasing luminosity phase would show an OVIII absorption edge correlated with the intensity of the ionizing continuum, as seen in MGC-6-30-15 (Fabian et al., 1994, Reynolds et al., 1995). At this density CVII is able to reach its maximum equilibrium value (Fig. 6b), but even this ion does not relax to its initial equilibrium value for many times up and down cycle time. Fig. 6b also shows that the ions reach their maximum values at different times. n_{CVII} reach its maximum value about 4,000 s before n_{OIX} .

At higher densities ($n_e = 10^9 \text{ cm}^{-3}$, dashed lines), the fractional abundance of each of the three ions reaches its maximum equilibrium value during the first 6,000 s, and relaxes to its minimum equilibrium value during the following 2.4×10^4 s, but with different timescales: OIX reaches its minimum equilibrium value after a time corresponding to two cycles, about one cycle after CVII. This could help to explain why models in which all ions of all elements are in photoionization equilibrium, so often fail to describe AGN spectral evolution. Spectra accumulated immediately after a very steep decreasing intensity phase could contain no significant absorption features at the energies of OVII–OVIII K-edge (the oxygen being completely ionized), but still show a deep absorption edge at $E \sim 0.5$ keV, due to the presence of a large amount of recombined CVI–CVII in the absorbing gas. High quality spectra would allow powerful tests of non-equilibrium photoionization models.

A general result is that the observation of any delays in the response of the absorber to flux changes on time scales of $\sim 5000 - 1000$ s, immediately implies photoionization with a density in a reasonably restricted range, $10^6 \lesssim n_e \lesssim 10^9 \text{ cm}^{-3}$ (depending on the average ionization state).

3. Modeling the ROSAT data of NGC4051

As an example of applicability of our models we present here the case of a ROSAT PSPC observation of the low luminosity, rapidly variable Seyfert 1 galaxy NGC4051.

Both the soft and hard X-ray flux of NGC4051 vary by large factors (up to 20) on a time scale of hours (e.g. Lawrence et al., 1985, Guainazzi et al., 1996) in a roughly correlated way. The presence of an ionized absorber in this source was first proposed on the basis of variations of the GINGA softness ratio correlated with the flux (Fiore et al. 1992). ROSAT PSPC

observations, and subsequently observations with the higher resolution CCDs on board of the ASCA satellite (Pounds et al. 1994, Mc Hardy et al. 1995, Mihara et al. 1994, and Guainazzi et al. 1996), also suggested the presence of a high column density, highly ionized absorber through the detection of a deep absorption edge at 0.8-0.9 keV.

McHardy et al. (1995), find that a simple single zone equilibrium photoionization model can provide a reasonably good representation of spectra accumulated in 1000-3000 seconds, but the best fit ionization parameter does not track the source intensity, as required by the model. This behaviour cannot be explained in a single zone ionization equilibrium model and therefore NGC4051 is a good target to test our time-evolving photoionization and collisional ionization models. We decided to compare our models to the ROSAT PSPC data acquired on 1991 November 16, and reported by McHardy et al. (1995), when the source count rate showed large and rapid variations (up to a factor of 6 in a few thousand sec., see figure 5 of McHardy et al., 1995). Analysis of the ASCA observation is deferred to a future publication.

The data reduction and the timing analysis were performed using the PROS package in IRAF. The observation spanned 77 ksec and contained 28.7 ksec of exposure time. NGC 4051 gave a mean count rate of 1.6 s^{-1} . We accumulated eight spectra ($a - h$), using a 3' radius extraction region, accumulating contiguous data with similar count rates. Background counts and spectra were accumulated from an annulus of internal and external radius of 3'.5 and 6' respectively.

3.1. Hardness ratio analysis: the absorber is not in photoionization equilibrium

Independent of any spectral fit the behavior of the main physical properties of the absorber can be seen in a color-color diagram. In Fig. 7 we plot the hardness ratios $HR=H/M$ against the softness ratio $SR=S/M$ from the count rates in three bands ($S=0.1-0.6 \text{ keV}$, $M=0.9-1.5 \text{ keV}$, and $H=1.7-2.5 \text{ keV}$) for theoretical curves (for $\log(N_H)=22, 22.5$ and 23) obtained by folding the equilibrium photoionization models (for $\log(U)$ in the range -0.3 to $+1.5$, and Galactic $N_H: 1.31 \times 10^{20} \text{ cm}^{-2}$, Elvis et al. 1989) with the response matrix of the PSPC. We also plot the colors of the source in the eight spectra ($a - h$). All the data points lie in a region of this diagram corresponding to the high U ends of the photoionization theoretical curves where both SR and HR decrease, as U increases, until all the ions in the gas are full stripped and the gas is completely transparent to radiation of any energy. The colors of NGC 4051 are all consistent with the OVIII-OIX ions being dominant. Filled circles on the $\log N_H=22.5$ curve mark values of U in the range 4.0–7. All the data points are between

the two extreme values of U , a factor ~ 1.5 change, while the source intensity varies up to a factor ~ 6 in the eight spectra. The gas is clearly not responding to the continuum variations, a conclusion equivalent to that obtained by McHardy et al. (1995) using spectral fits with equilibrium photoionization models (see their figure 5). In the framework of the models discussed in this paper this behavior suggests three different possibilities (we do not take in account pure collisional ionization in this case because the observed spectral variations should be attributed to ‘ad-hoc’ changes of T_e or N_H on time scales as short as 2000-4000 s):

1. the gas is far from ionization equilibrium;
2. the gas has a distribution of densities;
3. both collisional and photoionization processes are comparably important in the same physical region.

We investigated these possibilities in turn using detailed spectral fits.

3.2. Time-evolving photoionization

From Fig. 1 we see that a given ionization state can be roughly determined by the measure of at least two consecutive ion abundances, e.g. OVII and OVIII. The measure of a single edge in fact would not distinguish between ‘low’ and ‘high’ ionization solutions. The same measured feature could be produced by a lower N_H , lower mean ionization gas, or by an higher N_H , higher mean ionization state gas.

The best derived quantities to compare observed spectra with our several physical models are atomic edge strengths. Here we are mainly interested in the OVII and OVIII because they are the strongest and therefore the easiest to detect and measure. However, with the PSPC OVII and OVIII edges are not individually discernable, and we must resort to model fits with multiple components. Our choice is to use the components that can ensure an estimate of the OVII and OVIII τ as unbiased as possible.

3.2.1. A 3-edge ‘Model Independent’ Spectral Fit

We fitted the eight spectra with a model consisting of a power law reduced at low energy by the Galactic column density, the OVII and OVIII edges and another edge at 1.36 keV to account for possible spectral complexity in the 1-2 keV region (in particular the NeIX-X K and Fe XV-XX Lp absorption discussed in §2.1). Five parameters were at first allowed to be free to vary: the spectral index α_E , the OVII and OVIII edges τ , the 1.36 keV edge τ and the model normalization. The results are presented in Table 3. The fits with the 3 edges model are acceptable in all cases. We stress that $\tau(1.36 \text{ keV})$ in Table 3 should not be regarded as a true measure of the optical depth of Ne K and Fe L ions. This feature provides only one of the possible parameterizations of the spectrum in the 1-2 keV range, a band in which a change in the continuum spectral index could also be present (the 2-10 keV Ginga and ASCA spectra of this source are typically flatter by ≈ 0.5 than the PSPC 0.1-2 keV spectra). As discussed in §2.1 is difficult to discriminate between Ne absorption and a real spectral flattening above 1 keV with instruments of moderate spectral resolution like the PSPC. We have performed a series of fit using a broken power law with break energy in the 1-2 keV band and the two oxygen edges, obtaining τ similar to those reported in Table 3. We are therefore confident that the estimation of the oxygen edge τ is robust, within the rather large uncertainties given in Table 3. In principle, a way to reduce the uncertainties is to fix the continuum spectral index to a common value. The results of this series of fits are again given in Table 3. The uncertainties on $\tau(\text{OVII})$ and $\tau(1.36 \text{ keV})$ are indeed smaller than in the previous case but this is not true for the $\tau(\text{OVIII})$ uncertainties. The reason is that there is a strong anti-correlation between α_E and τ_{OVII} . A similar anti-correlation is present between α_E and $\tau(1.36 \text{ keV})$. In contrast no correlation is present between α_E and $\tau(\text{OVIII})$. This is illustrated in Fig. 8 where we show the χ^2 contours of these parameters for spectrum *g*. Since the $\tau(\text{OVII})$ values could be biased in the fit with fixed α_E by the $\tau(\text{OVII})$ - α_E correlation, we prefer to compare our time-evolving models to the OVII and OVIII optical depths obtained leaving α_E free to vary.

In all but one case (spectrum *d*) the depth of the OVIII edge is higher or comparable to that of OVII, suggesting a ‘high’ ionization solution ($U > 4$, see Fig. 1), consistent with the hardness ratio analysis of Fig. 7.

3.2.2. Comparison between models and the oxygen edge depths: evidence for a non-equilibrium photoionization absorber?

We converted the best fit τ into OVII and OVIII relative abundances assuming a solar oxygen abundance and a total hydrogen column density N_H . An indication of N_H comes from

Table 1: **NGC 4051: 3-Edge Model Fits**

Spectrum	$\tau(0.74 \text{ keV})$	$\tau(0.87 \text{ keV})$	$\tau(1.36 \text{ keV})$	α_E	$\chi^2(\text{d.o.f.})$
a	$0.5^{+0.5}_{-0.4}$	$0.84^{+0.32}_{-0.33}$	1.0 ± 0.4	1.3 ± 0.1	0.84(21)
	$0.34^{+0.29}_{-0.23}$	$0.84^{+0.31}_{-0.32}$	$0.81^{+0.28}_{-0.23}$	1.34 (fixed)	0.82(22)
b	< 0.5	0.66 ± 0.21	0.7 ± 0.3	1.3 ± 0.1	1.19(23)
	$0.23^{+0.19}_{-0.16}$	0.66 ± 0.21	$0.71^{+0.18}_{-0.16}$	1.34 (fixed)	1.14(24)
c	$0.5^{+0.5}_{-0.4}$	$0.41^{+0.31}_{-0.34}$	< 0.6	1.3 ± 0.1	0.85(22)
	$0.38^{+0.33}_{-0.26}$	$0.41^{+0.31}_{-0.34}$	< 0.42	1.34 (fixed)	0.82(23)
d	< 0.7	< 0.3	$1.1^{+0.8}_{-0.6}$	$1.6^{+0.1}_{-0.2}$	0.95(18)
	$0.99^{+0.22}_{-0.35}$	< 0.32	$1.95^{+0.81}_{-0.54}$	1.34 (fixed)	1.08(19)
e	$0.5^{+0.4}_{-0.3}$	0.86 ± 0.28	0.5 ± 0.3	1.4 ± 0.1	1.30(22)
	$0.62^{+0.28}_{-0.22}$	$0.86^{+0.28}_{-0.30}$	0.65 ± 0.19	1.34 (fixed)	1.25(23)
f	< 0.6	$1.01^{+0.24}_{-0.23}$	< 0.5	1.4 ± 0.1	1.41(23)
	$0.54^{+0.20}_{-0.18}$	$1.02^{+0.23}_{-0.25}$	0.44 ± 0.14	1.34 (fixed)	1.42(24)
g	< 0.5	1.47 ± 0.29	< 0.5	1.3 ± 0.1	0.65(22)
	< 0.18	$1.42^{+0.16}_{-0.24}$	< 0.21	1.34 (fixed)	0.67(23)
h	$1.2^{+0.6}_{-0.5}$	$0.79^{+0.35}_{-0.42}$	$0.9^{+0.4}_{-0.3}$	1.2 ± 0.1	0.72(22)
	$0.63^{+0.33}_{-0.25}$	$0.86^{+0.33}_{-0.35}$	$0.45^{+0.20}_{-0.19}$	1.34 (fixed)	0.82(23)

the color-color diagram of Fig. 7. Although calculated using a photoionization equilibrium model, the theoretical curves in this diagram suggest a value for $\log N_H$ between 22 and 23, and so we adopt $\log N_H = 22.5$. The three panels of Fig. 9 show the light curves of the source count rate (upper panel) and of the OVIII and OVII abundances (middle and lower panels respectively).

The time evolution of the ionization structure of a cloud of gas photoionized by a variable source is complex and its behaviour sometime counter-intuitive. We then discuss first the simplest case: high electron density, for which each ion is close to its equilibrium state. We examine next the case of lower densities and hence non-equilibrium solutions.

The dotted curves on the middle and lower panels of Fig. 9 show the $n_e = 10^{10} \text{ cm}^{-3}$, $P=1$ (the ratio of the incident flux to that needed to produce the initial ionization distribution assuming photoionization equilibrium) curves, when the gas is close to equilibrium. While the equilibrium OVII curve tracks the count rate variations (it is strictly anticorrelated with the count rate light curve), the OVIII curve does not. The different OVIII behaviour is due to the different balance in the destruction rates of OIX and OVIII. When the ionizing flux is at its maximum most of the oxygen is OIX. When the flux decreases from the maximum (from point *b* to *d*) OIX recombines to OVIII increasing the OVIII abundance. When the flux decreases from point *e* to point *f* at first OVIII increases again because of the high destruction rate of OIX, but after a certain point the amount of OVIII recombining to OVII start to be higher than the amount of OIX recombining to OVIII, and so the total OVIII abundance start to decrease. Instead, the amount of OVIII recombining to OVII is always higher than the amount of OVII recombining to OVI. This gives rise to a different behaviour of the OVIII and OVII curves in response to the same ionizing flux variations. It is interesting to note that in this case while the dynamical range of variation of the OVII curve is larger than that of the ionizing flux, the OVIII equilibrium curve shows a more compressed range of variations (when the ionizing flux varies by a factor of 6 the OVIII and OVII abundances vary by a factor of 3 and 30 respectively, see Fig. 9). Therefore variations of OVIII would be much more difficult to detect than variations of OVII, at least at these regimes of ionization. We re-emphasize: *the behaviour of a single edge does not provide a unique interpretation of the data.*

As explained in §2.3.3, a grid of theoretical OVII and OVIII light curves was generated using our time-evolving photoionization code for 28 values of n_e from $5 \times 10^6 \text{ cm}^{-3}$ to 10^9 cm^{-3} and 15 values of P from 0.5 to 2.

We compared these curves with the measured relative abundances of OVII and OVIII and found the best fit model using a χ^2 technique. The thick solid lines in the lower and middle panels of Fig. 9 represent the best fit non-equilibrium OVII and OVIII curves. The agreement

between the best fit model and the observed OVII and OVIII abundances is good: $\chi^2 = 1.17$ for 14 dof. The best fitting values for n_e and P are tightly constrained: $n_e = (1.0_{-0.5}^{+1.2}) \times 10^8 \text{ cm}^{-3}$, $P = 1.5_{-0.3}^{+0.4}$. From the best fit n_e we can estimate the distance of the absorbing cloud from the central source. We obtain $R = (0.74_{-0.40}^{+0.80}) \times 10^{16} \text{ cm}$ (3 light days).

The dashed lines represent the solutions obtained using the 1σ confidence interval on n_e and P. The best fit curves (and the 1σ confidence intervals curves) show a compressed dynamical range of OVIII and OVII abundances variations and a delay between the source maxima and the ion abundance minima of 3000-6000 sec. The compressed dynamical range is due to a mean over-ionization of the gas. While the best fit P shows that the gas in the initial point *a* is near to equilibrium, it departs strongly from equilibrium during the later low intensity states (spectra *d* to *h*). So, despite the fact that the source spends more time in low states than in high states, the gas density is sufficiently low that the gas does not have time to fully recombine after the few events when it suffers high illumination and becomes highly ionized.

The above results were obtained assuming a total hydrogen column density of $\log(N_H) = 22.5$. Assuming an higher (lower) column would imply a mean lower (higher) OVII and OVIII relative ion abundance. Therefore, in principle the accurate measure of both edges would constrain also the total warm column density. The uncertainties on the PSPC determinations however preclude this possibility, and better resolution measurements are therefore needed. The energy resolution of the ASCA SIS, for example, is just sufficient to separate the OVII and OVIII absorption edges. A quantitative test of non-equilibrium photoionization model using the ASCA data and a comparison between ROSAT PSPC and ASCA data of NGC 4051 is beyond the scope of this paper and will be presented in a future publication. A much better separation, and therefore characterization, of the absorption features will be possible with the high resolution (factor of 10-30 better than ASCA SIS) gratings on AXAF and XMM.

3.3. Other models

Despite the success of time-evolving photoionization models, alternatives do exist. We discuss two of them in the following.

3.3.1. Large density variations in the absorbing gas

If the gas is not confined to a single cloud with constant density but rather is distributed in a region with, say, an increasing density, then different ionization equilibria could apply to different regions in the cloud. Two extreme regions may exist: in the region with higher density, lower U , collisional ionization will be the dominant ionization mechanism and the spectra transmitted by this region would show always the same features, irrespective of the source intensity; the other region, with lower density and higher U , is completely ionized (for carbon, oxygen, neon and iron ions up to FeXXII) when the source is in the high state, but when the source is in a low state the abundances of OVIII are sizeable and imprint the edges in the spectrum seen in low intensity spectra. Here we are assuming that the density of the photoionized region is high enough for the gas to be in instantaneous equilibrium with the ionizing intensity. If not, the average ionization degree of the gas would be very high during the whole observation, and the gas would be always almost transparent at the energies of the relevant absorption edges.

We tested this hypothesis by fitting the highest intensity spectrum (*b*) with a simple power law model plus a collisionally ionized absorber, using the method of Fiore et al. (1993). The best fit temperature and N_H are $2.8 \pm 0.1 \times 10^6$ K and $1.5_{-0.5}^{+0.7} \times 10^{22} \text{cm}^{-2}$ respectively. We then used the same model (with fixed continuum parameters, fixed temperature and N_H but variable normalization) with the inclusion of an additional OVIII edge to mimic a variable ionization state, equilibrium photoionization absorber. The fits are all acceptable. The worst fit is that of spectrum (*d*) ($\chi^2 = 1.4$, 21 dof, probability of 10.4 %). In Fig. 10 we plot $\tau(OVIII)$ as a function of the time. The dynamic range of variations of τ is here larger than that on n_{OVIII} in Fig. 9 but is still more compressed than that predicted by equilibrium photoionization model (solid line). We can therefore exclude the possibility that a major part of this absorber could be in pure photoionization equilibrium with the ionizing intensity.

3.4. A “hot” photoionized absorber

The other possibility is that both collisional and photoionization processes are important in the same physical region. In this case the transmitted spectra are very similar to those transmitted from purely photoionized clouds of gas which much higher ionization parameter (§2.1, Fig. 4). The electron temperature of the gas is mainly determined by collisions, and is higher than that expected in pure photoionization equilibrium. The ionization parameter U is no longer linearly correlated with the ionizing intensity, and then its dynamical range of variations is compressed by a factor > 2 compared to the pure photoionization case.

This could in principle explain the compression observed in the measured dynamical range of variation of n_{OVIII} , but could not account for the delays observed on the response of the ionization state of the gas to source intensity variation. Unfortunately there is no way to distinguish between ‘hot’ photoionized absorber models and simple pure photoionization models on the only basis of the spectral analysis. Nevertheless the delay observed in the response of the ionization degree of the gas between spectrum (b) and (c) suggests that a non-equilibrium photoionization component is mainly required by data.

4. Conclusion

We have investigated ionization models for AGN in different regimes of gas volume densities and photoionization states. In particular we focussed on ‘high gas density, low photoionization parameter’ gas clouds, where collisional ionization is likely to play a significant role in the gas ionization, and on low gas densities, where the photoionization may be far from equilibrium.

We presented detailed model calculations in both regimes. While the time-evolving photoionization models in §2.3 are far from being complete or exhaustive they are nevertheless instructive, and reveal the main features of these kinds of models.

Our main findings can be summarized as follows:

1. In many important astrophysical conditions (OVII, OVIII regime) the fractional abundances of the most important ions of O and Ne in photoionized gas are more broadly distributed in U than those of collisionally ionized gas are in T .
2. In the collisional ionization case the heavy elements show a strong inertia against becoming highly ionized, even when lighter elements, like Oxygen, are almost fully stripped. In this case the transmitted spectrum shows a large and complicated absorption structure between 1 and 3 keV, mainly due to iron L XVII-XIX and Neon K IX-X absorption, which is much less visible in spectra emerging from photoionized gas with similar OVII and OVIII abundances. This absorption structure may be mis-interpreted as a flattening of the spectra above ~ 1 keV, when fitting low energy resolution data with a photoionization equilibrium model. Higher spectral resolution and good S/N observations are therefore needed to distinguish between collisional ionization and photoionization.

3. In non-equilibrium photoionization models the response of the ionization state of the gas to sudden changes of the ionizing continuum is delayed even during increasing luminosity phases. The delays increase for decreasing electron densities, as changes of n_e , require changes of the intensity of the ionizing flux, i.e. changes of the distance of the gas from the X-ray source (taking as fixed the initial ionization state of the gas).
4. The recombination timescale is generally much longer (up to orders of magnitudes) than the photoionization timescale, because of the dependence of $t_{eq}^{X^i, X^{i+1}}(t \rightarrow t + dt)$ on the equilibrium ratio ($n_{X^{i+1}}/n_{X^i}$), evaluated at the time $t + dt$. This means that a photoionized absorber undergoing frequent, quick, and consistent changes of ionizing luminosity is likely to be overionized with respect to the equilibrium ionization, a state that would be reached only after a sufficiently long low intensity phase.
5. If the changes of the ionizing luminosity are not instantaneous, and the electron density of the cloud is low enough, the ionization state of the gas could continue to increase during decreasing source luminosity phases. This means that we may measure a maximum in ionization state of a given element, when the ionizing flux is at a minimum (opposite to what is expected in equilibrium models).
6. Different ions of different elements reach their equilibrium abundance on different timescales. This is again because of the dependence of $t_{eq}^{X^i, X^{i+1}}(t \rightarrow t + dt)$ on the ratio ($n_{X^{i+1}}/n_{X^i}$). Therefore in the same cloud of gas carbon could be in equilibrium while oxygen could be very far from equilibrium. This may help in explaining why models where *all ions of all elements* are in photoionization equilibrium so often fails to provide a reasonable description of AGN spectra and spectra evolution

We have tested the above models in the case of the Seyfert 1 galaxy NGC4051. The ROSAT observations of NGC4051 are not consistent with a simple equilibrium model, but can be explained straightforwardly by our time-evolving photoionization models. The two main features in the non-equilibrium best fit models are: (a) the compressed range of variability of the measured OVII and OVIII relative abundances with respect to the amplitude of the source variations, and to the amplitude of the variations of the abundances of these ions expected in equilibrium photoionization models; (b) the 3000-6000 sec delay between the maximum intensity state of the source (spectrum *b*) and the minimum of the best fit OVIII abundance curve, i.e. the maximum ionization state of the gas (spectrum *c*). As result we were able to estimate the gas electron density, $n_e = (1.0_{-0.5}^{+1.2}) \times 10^8 \text{ cm}^{-3}$ (assuming $\log N_H = 22.5$) and hence the distance of the ionized gas cloud from the X-ray source in $R = (0.74_{-0.40}^{+0.80}) \times 10^{16} \text{ cm}$ (3 light days). We explored alternative models and we also explored alternatives which we find to be less likely; we discuss ways to distinguish between them conclusively.

We conclude that non-equilibrium photoionization and collisional models apply to wide zones of gas density and ionization, zones which are expected in AGN. These effects must be considered in understanding ionized absorbers, and seem likely to explain otherwise puzzling behavior, without resorting to ad hoc distributions of gas. Several clear diagnostics of these models exist so that decisive tests will soon be possible.

We thank Giorgio Matt for useful discussions. We also thank an anonymous referee whose comments contributed to improve the manuscript. This work was supported in part by NASA grant NAG5-3066 (ADP). F.F. acknowledges support from NASA grant NAG5-2476. This work made use of the IRAS/PROS package and the ROSAT archive maintained at the HEASARC.

REFERENCES

- Arav N., Korista K.T., Barlow T.A., Begelman M.C., 1995, *Nature*, 376, 576
- Binette L. & Robinson A., 1987, *A&A*, 177, 11
- Binette L., 1988, 185, *proceedings of the AGN Conference*, Atlanta, Georgia (US), 1987, *pub.: Springer-Verlag*
- Brandt W.N., Fabian A.C., Nandra K., Reynolds C.S., Brinkmann W. 1994, *MNRAS*, 271, 958
- Cappi M., Mihara T., Matsuoka M., Hayashida K., Weaver K.A., Otani C. 1996, *ApJ*, 458, 149
- Done C. et al. 1990, *MNRAS*, 243, 713
- Done C., Pounds K.A., Nandra K., Fabian A.C. 1995, *MNRAS*, 275, 417
- Elvis M., Wilkes B.J., Lockman F.J., 1989, *A.J.*, 97, 777
- Fabian A.C. et al. 1994, *PASJ*, 46, L59
- Ferland G.J., 1996 CLOUDY: 90.01
- Fiore F., Perola G.C., Matsuoka M., Yamauchi M., Piro L. 1992, *A&A*, 262, 37
- Fiore F., Elvis M., Mathur S., Wilkes B.J., McDowell J.C. 1993, *ApJ*, 415, 192
- Gallavotti G. 1986, “The elements of mechanics”, *Boringhieri*, 2nd edition.
- George I.M. et al. 1995, *ApJ*, 438, 120
- George I.M., et al., 1997, *ApJ*, 491, 508

- George I.M., Turner T.J., Mushotzky R.F., Nandra K., Netzer H., 1998, ApJ, in press
- Grevesse N., & Anders E. 1989, “Cosmic Abundances of Matter”, AIP Conference Proceedings 183, ed. C.J. Waddington (New York: AIP).
- Guainazzi M., Mihara T., Otani C., Matsuoka M. 1996, PASJ, 48, 781
- Halpern J.P. 1984, ApJ, 281, 90
- Kallman T.R. & Krolik J.H. 1995, XSTAR: 1.10
- Kriss G.A. et al. 1996, ApJ, 467, 629
- Krolik J.H. & Kriss G.A. 1995, ApJ, 447, 512
- Laor, A, Fiore, F. Elvis, M., Wilkes, B.J. McDowell, J.C.M. 1997, ApJ, 477, 93
- Lawrence A., Watson M.G., Pounds, K.A., Elvis M. 1985, MNRAS, 217, 685
- Matsuoka M., Piro L., Yamauchi M., Murakami T. 1990, ApJ, 361, 440
- Mathur S., Wilkes B.J., Elvis M., Fiore F. 1994, ApJ, 434, 493
- Mathur S., Elvis M., Wilkes B.J. 1995, ApJ, 452, 230
- Mathur S., Wilkes B.J., Aldcroft T. 1997, ApJ, 478, 182
- Mathur S., Wilkes B.J., Elvis M., 1998, ApJL, submitted
- McHardy I.M. et al. 1995, MNRAS, 273, 549
- Mihara T. et al. 1994, P.A.S.J., 46, L137
- Nandra K. & Pounds K.A. 1992, Nature, 359, 215
- Netzer H. 1990, “Active Galactic Nuclei” ed. Springer-Verlag
- Nicastro F., Fiore F., Perola G.C., Elvis M., 1998, ApJ, submitted
- Nicastro F., Fiore F., Brandt W.N., Reynolds C.S., 1998, proceedings of *The Active Sky*, Rome, October 1997, *pub: Elsevier, The Netherlands*
- Orr A., Molendi S., Fiore F., Grandi P., Parmar A.N., Owens A., 1997, A&A, 324, 770
- Otani C. et al. 1996, P.A.S.J., 48, 211
- Pan H.C., Stewart G.C. & Pounds K.A. 1990, MNRAS, 242, 177
- Peterson B. 1993, P.A.S.P., 105, 247
- Pounds K.A., Nandra K., Fink H.H., Makino F. 1994, MNRAS, 267, 193
- Ptak T., Yaqoob T., Serlemitsos P.J., Mushotzky R., Otani C. 1994, ApJ, 436, L31
- Reynolds C.S. & Fabian A.C. 1995, MNRAS, 273, 1167

Reynolds C.S., Fabian A.C., Nandra K, Inoue H., Kunieda H, Iwasawa K. 1995, MNRAS, 277, 901

Reynolds C.S., 1997, MNRAS, 286, 513

Shastri P., Wilkes B.J., Elvis M., McDowell J. 1993, ApJ, 410, 29

Shull J.M. & Van Steenberg M. 1982, ApJS, 48, 95

Turner T.J., Nandra K., George I.M., Fabian A.C., Pounds K.A. 1993, ApJ, 419, 127

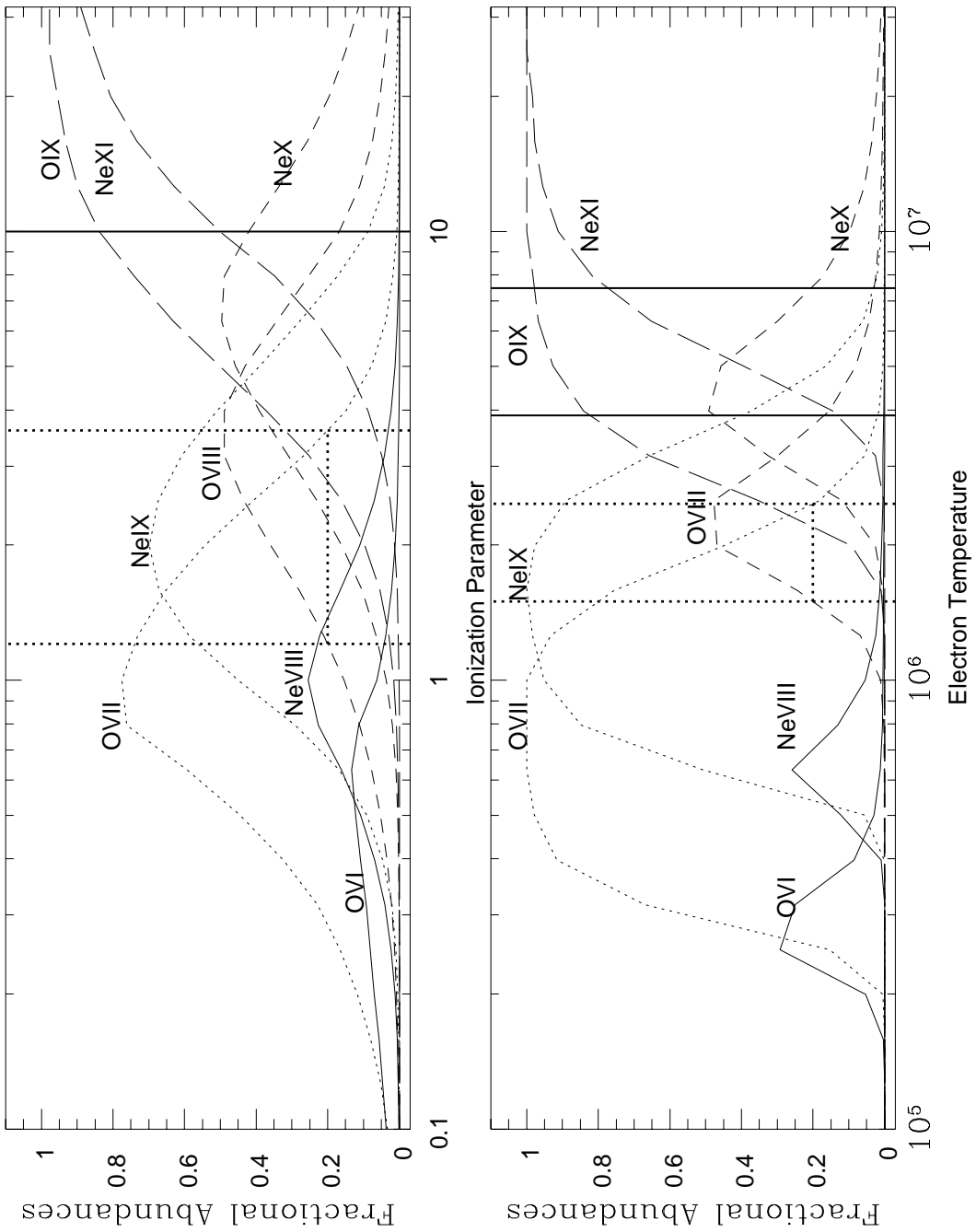
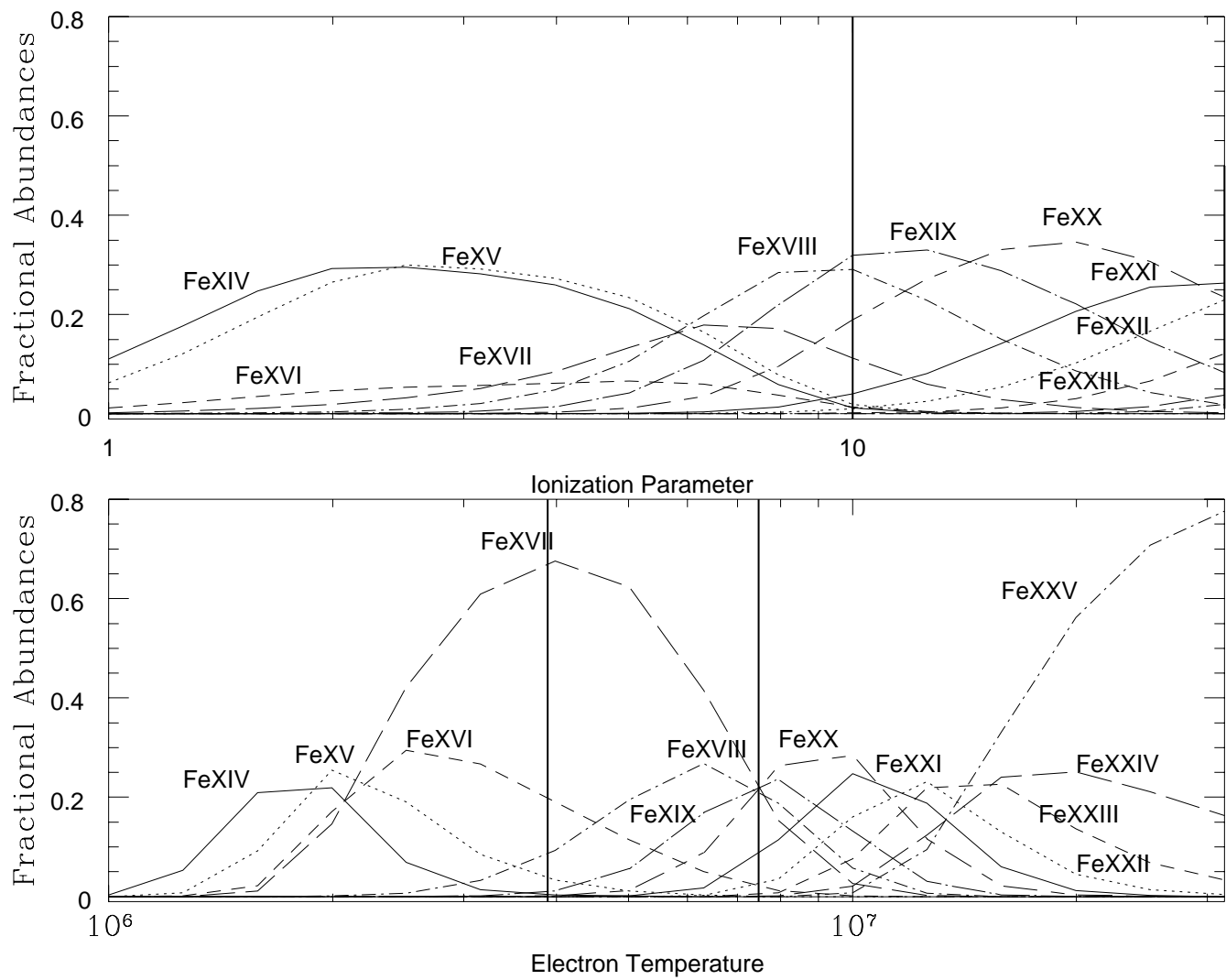


Fig. 1.— Fractional abundances of NeVIII-NeXI, and OVI-OVIX, calculated in the case of photoionization (Fig. 1a: upper panel), and collisional ionization (Fig. 1b: lower panel). The two intervals of U and T_e highlighted are: (a) the interval for which both OVII and OVIII abundances are greater than 0.2 (dotted lines), and (b) the one for which the OIX relative abundance is greater than 0.75.

Fig. 2.— Like Fig. 1, for the relative abundances of the ions FeXIV-FeXXV.



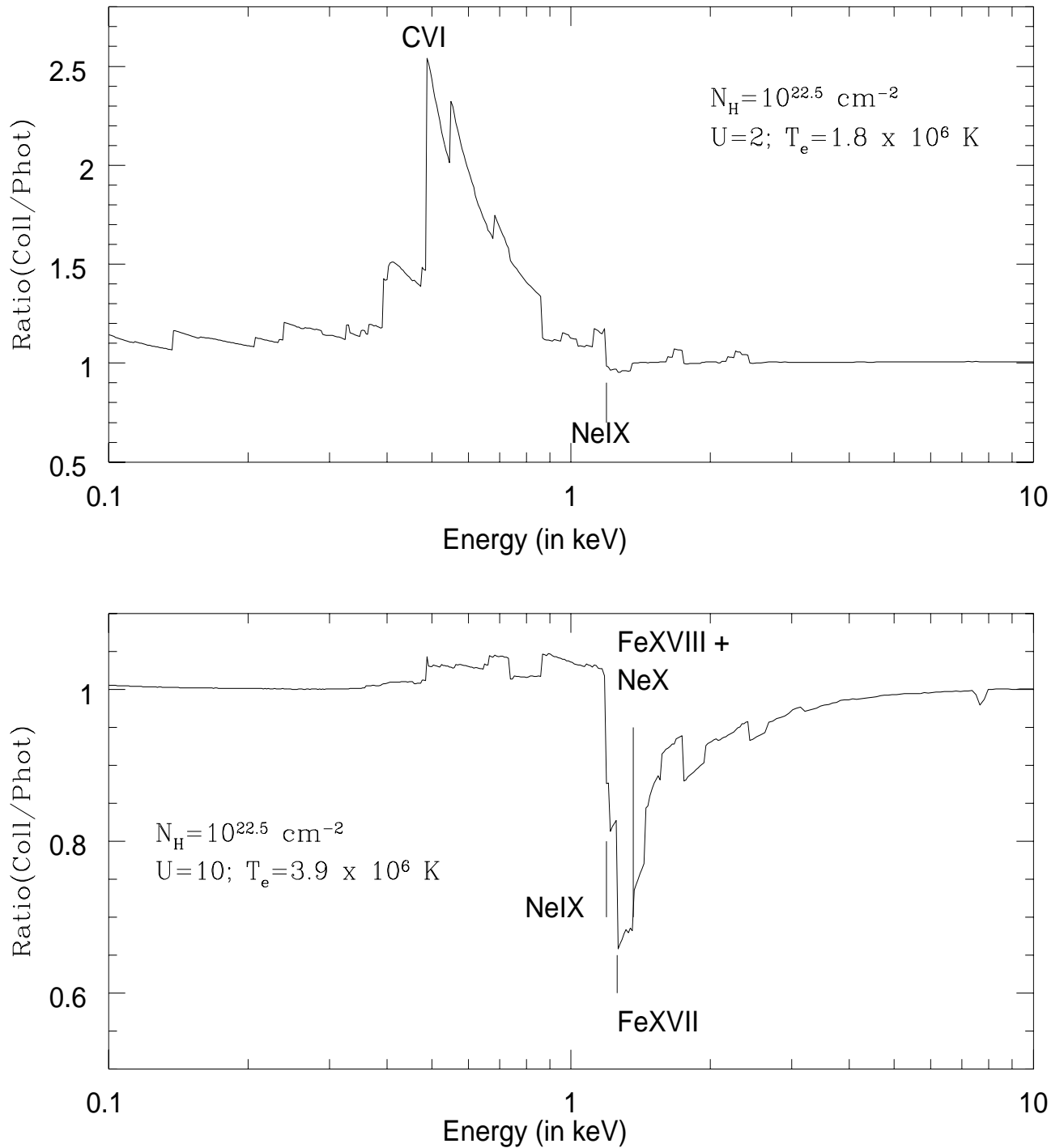


Fig. 3.— (a) The ratio between two power law spectra emerging from clouds of collisional ionized ($T_e = 1.8 \times 10^6 \text{ K}$) and photoionized ($U=2$) gas with solar abundances. (b) The ratio between two power law spectra emerging from clouds of collisionally ionized gas with $T_e = 3.9 \times 10^6 \text{ K}$, and photoionized gas with $U=10$. The column density is $N_H = 10^{22.5} \text{ cm}^{-2}$ in both cases.

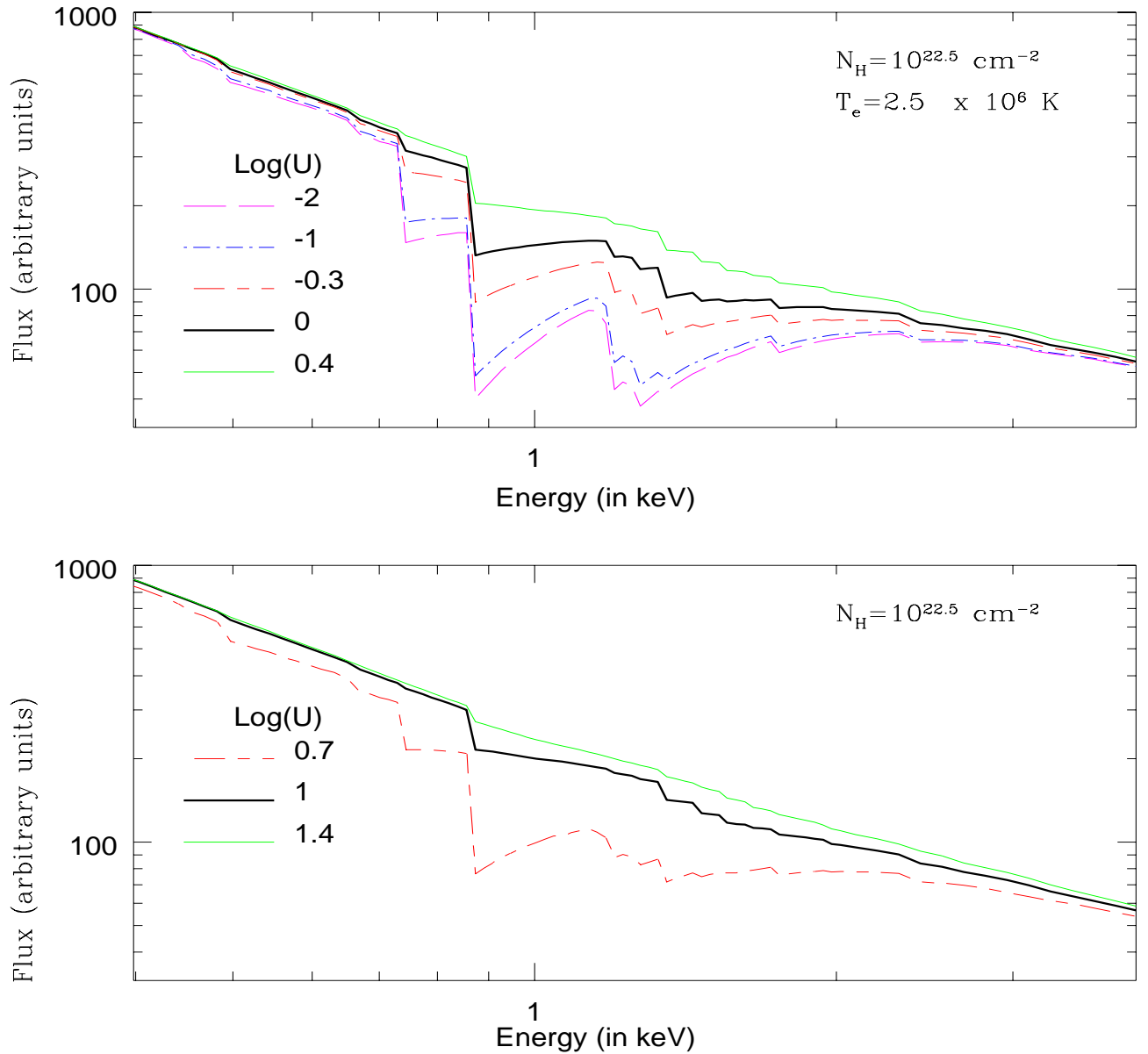


Fig. 4.— (a) Spectra from gas in which both collisional ionization and photoionization are important. The temperature of the gas is fixed at $T_e = 2.5 \times 10^6 \text{ K}$, and $\log(U) = -1, -1, 0.3, 0, 0.4$. (b) Spectra from gas in pure photoionization equilibrium., with $\log(U) = 0.7, 1.1, 1.4$. The column density is $N_H = 10^{22.5} \text{ cm}^{-2}$ in both cases.

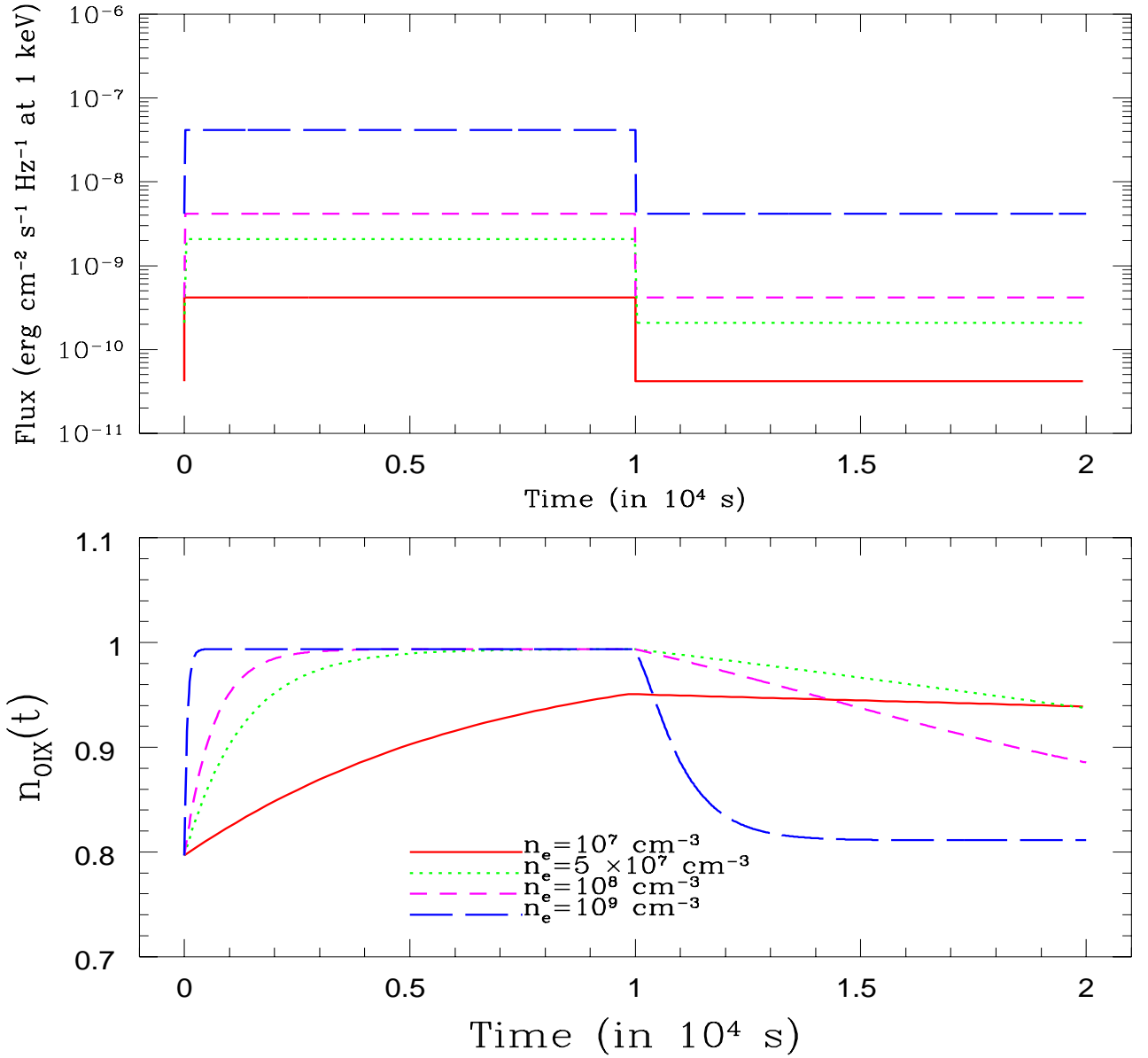


Fig. 5.— Upper panel: step light curve of the ionizing radiation, for four different values of the electron density ($n_e = 10^7$, 5×10^7 , 10^8 , and 10^9 cm^{-3} , which correspond to four different values of the incident flux). Lower panel: time behaviour of the relative abundance of OIX, for the four values of n_e .

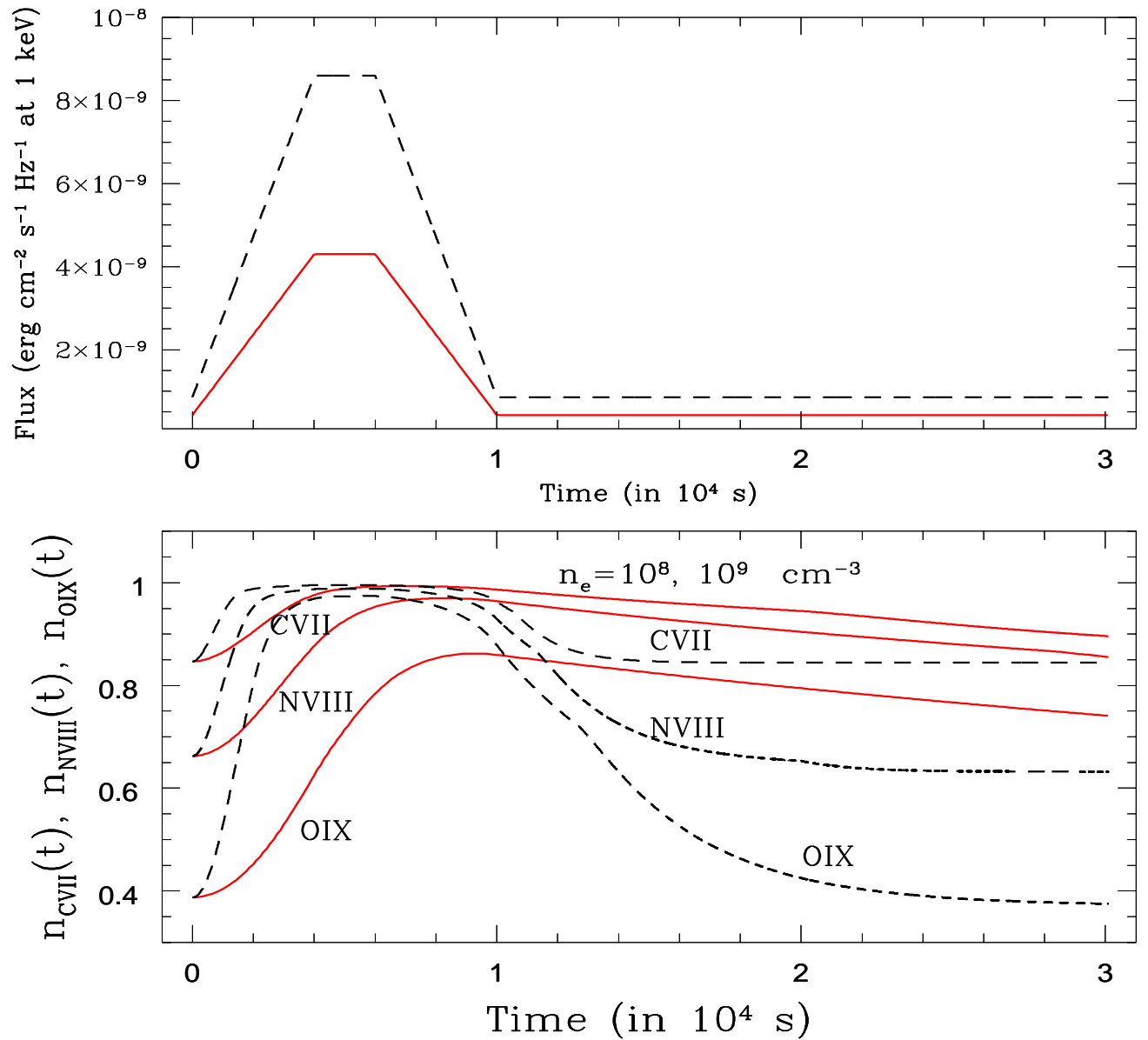


Fig. 6.— Upper panel: 2-phases light curve of the ionizing continuum. Lower panel: time behaviour of the relative abundances of the fully stripped ions of three elements: CVII, NVIII, OIX. In both panel different lines correspond to different values of the electron density, $n_e = 10^8$ (solid line), and 10^9 cm^{-3} (dashed line).

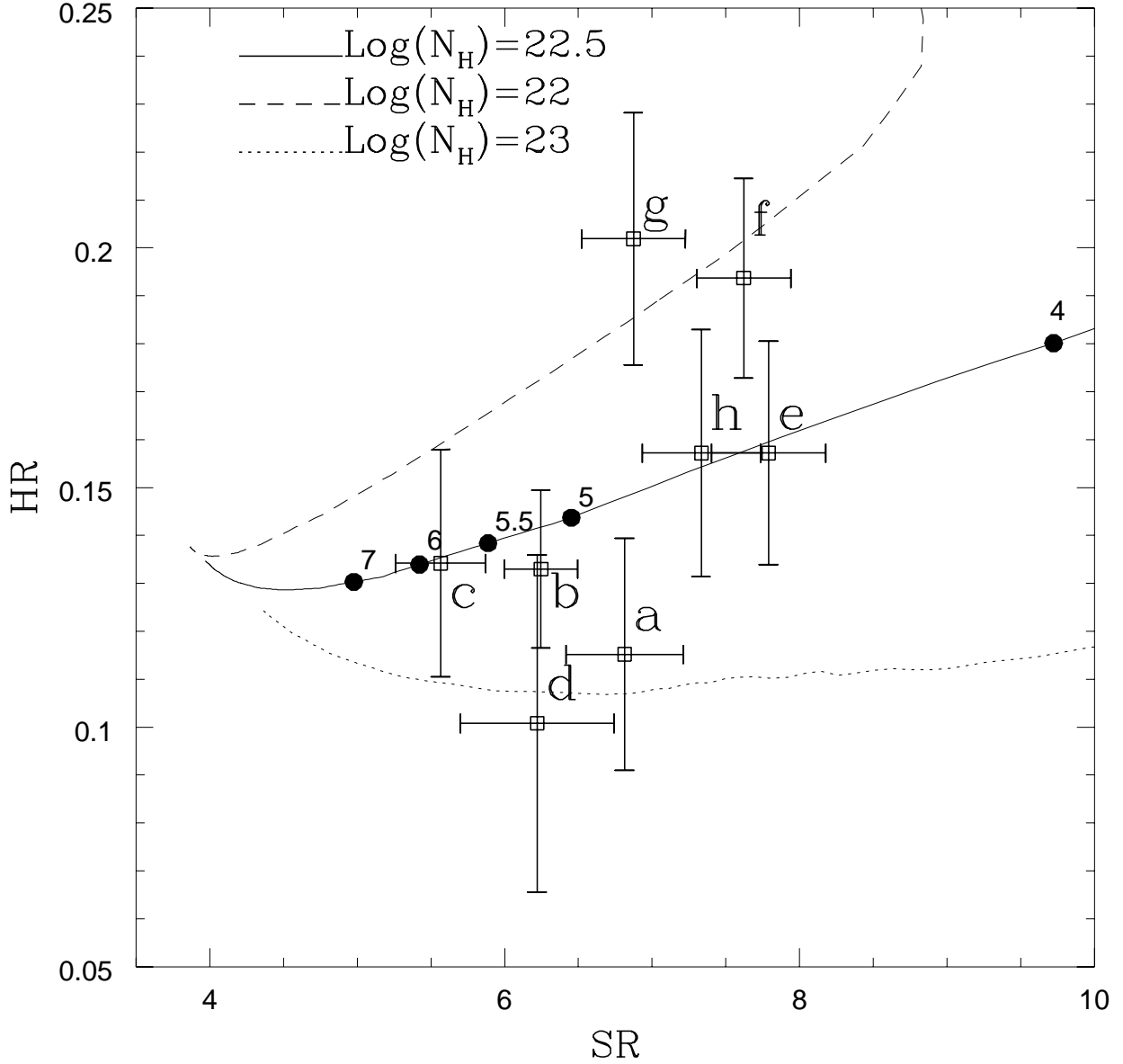


Fig. 7.— Color-color diagram of the eight spectra of NGC4051. Lines are theoretical photoionization curves, built folding equilibrium photoionization models with the response matrix of the PSPC. Different lines correspond to three different values of the gas column density: $\log(N_H)=22.5$ (solid line), $\log(N_H)=22$ (dotted line), and $\log(N_H)=23$ (dashed line). On each curve the ionization parameter U , increases going from top to bottom. U values are indicated on the $\log(N_H)=22.5$ line.

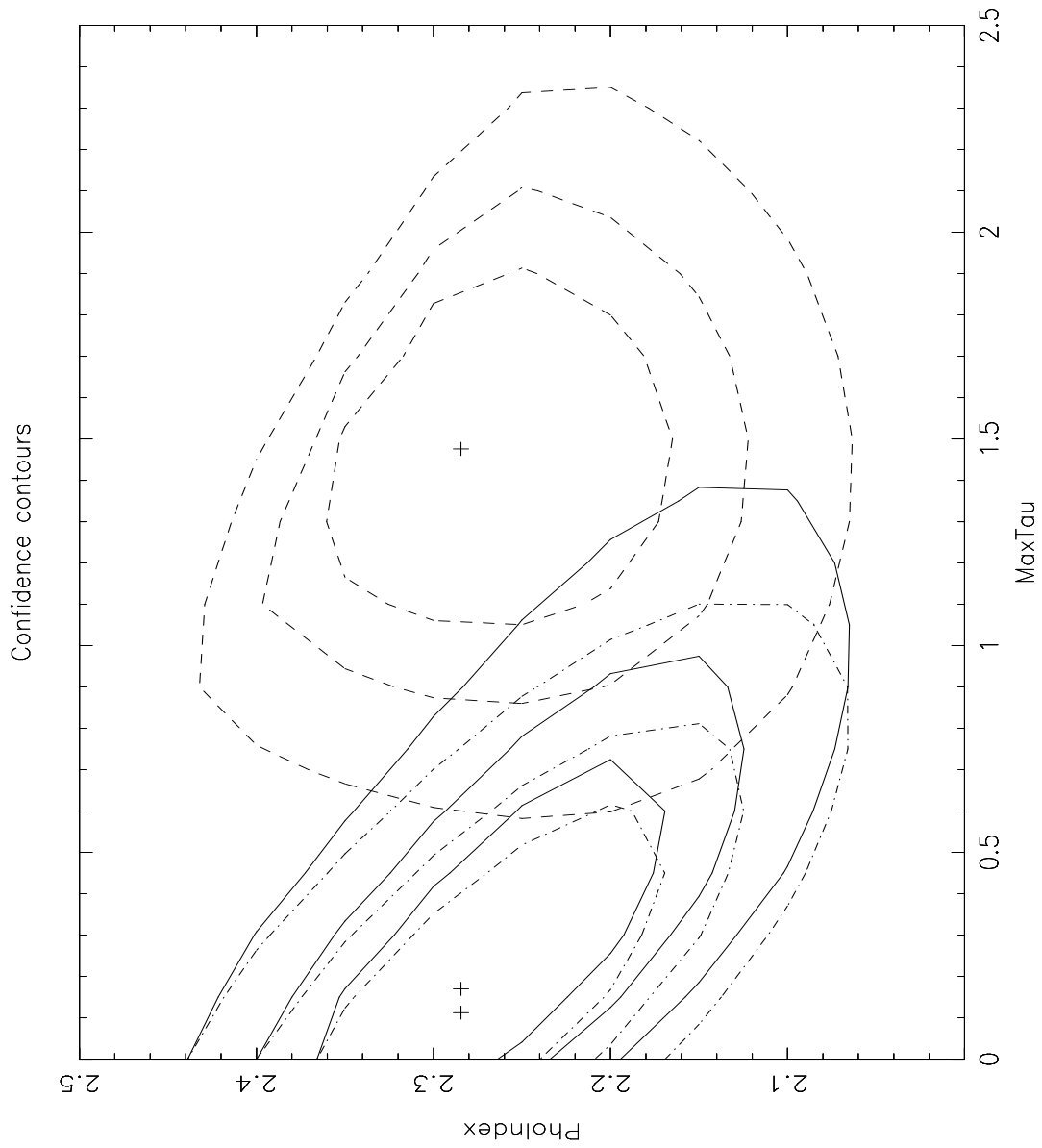


Fig. 8.— χ^2 contour plot of α_E and τ_{OVII} (solid curves) and α_E and τ_{OVIII} for spectrum g .

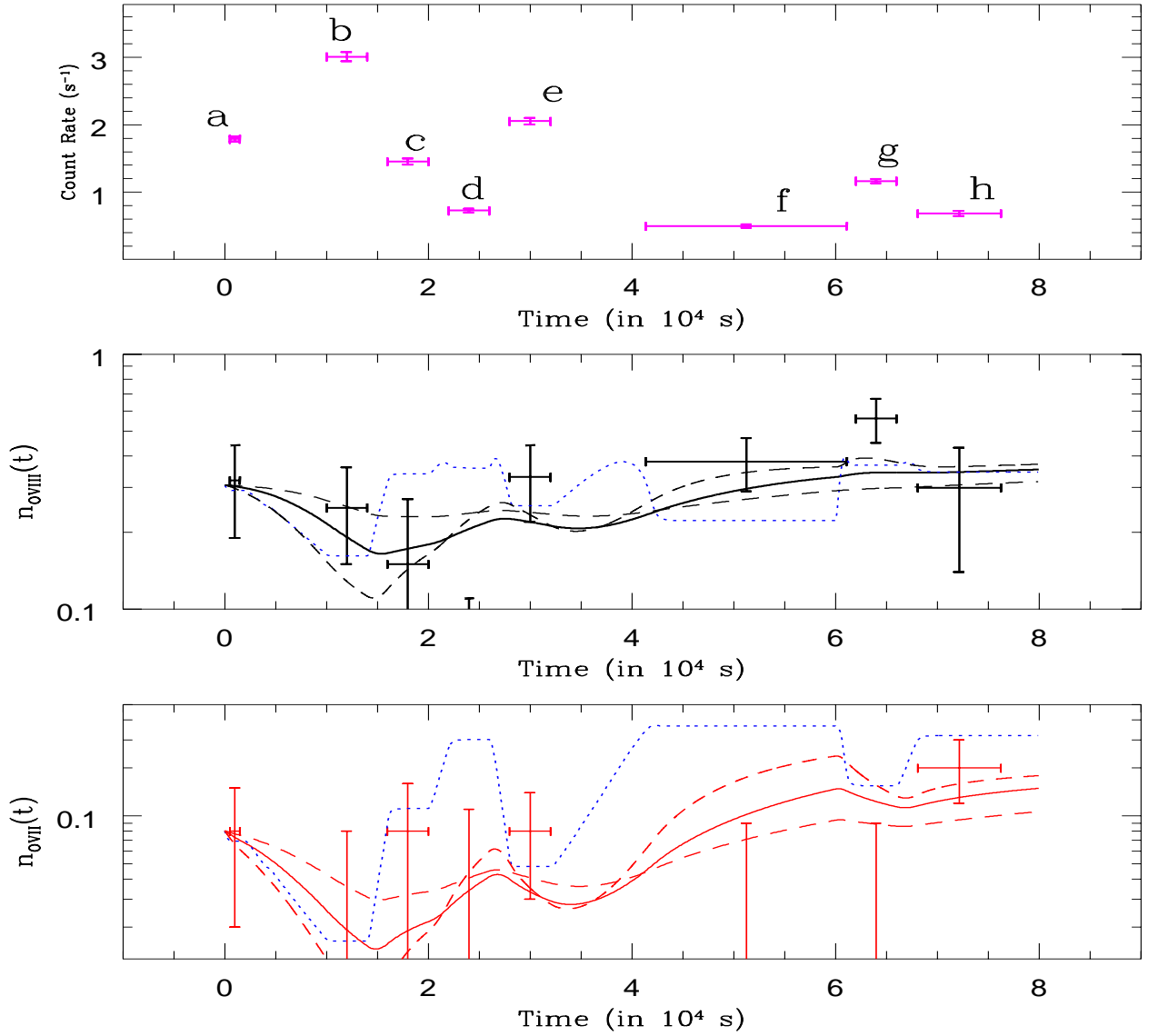


Fig. 9.— Light curve of NGC 4051 during the November 1991 ROSAT-PSPC observation (Upper panel). Middle and lower panel: Best fit n_{OVIII} and n_{OVII} abundances (points with errorbars), obtained by fitting a power law continuum plus 3-edge model to the 8 spectra, and by using $\log(N_H)=22.5$. Solid lines in the two panels represent the best fit non-equilibrium photoionization model to the n_{OVIII} and n_{OVII} data respectively, while dashed lines are the solutions obtained using the 1σ confidence interval on n_e e P. Dotted lines are the equilibrium n_{OVIII} and n_{OVII} curves, and was obtained using the non-equilibrium photoionization code by fixing $n_e = 10^{10} \text{ cm}^{-3}$ and $P=1$.

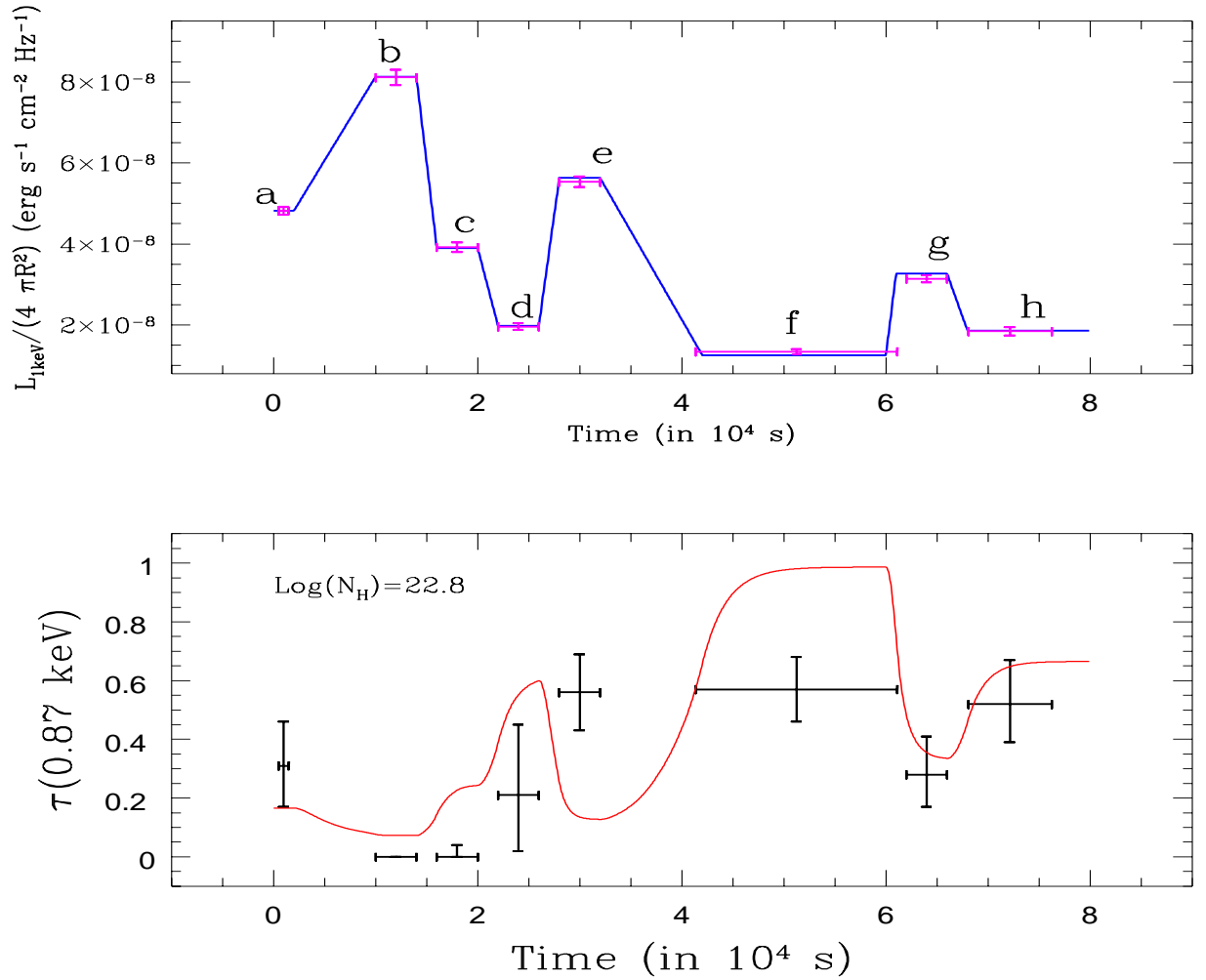


Fig. 10.— Similar to Fig. 9 but the lower panel shows the O VIII edge τ obtained fitting the eight spectra with a model consisting of a power law with energy index 1.3 (fixed in the fit) plus a collisional ionized absorber with $N_H = 1.5 \times 10^{22} \text{ cm}^{-2}$ and $T = 2.8 \times 10^6 \text{ K}$ (fixed in the fit) plus an edge at 0.87 keV. Two parameters only are allowed to vary: the model normalization and the O VIII edge τ .